

Indentation and Scratching on the Nanoscale



Herbert M. Urbassek, Iyad Alabd Alhafez, Hans Hasse, Michael Kopnarski, and Simon Stephan

Abstract Indentation and scratching of Fe, as a model of ferritic steels, are studied by atomistic simulation and experiment. The modeling allows to include the effect of lubrication. Selected experiments reveal the relevance of the nanoscopic simulation results to real surface scratching. We study the evolution of plasticity under indentation and scratching, the dependence of scratching on surface orientation and scratch direction, the influence of tip geometry on scratching, the effect of lubrication during scratching, and friction and wear on micro- and nanoscales.

1 Introduction

Indentation and scratching of surfaces are prototypical examples of the machining of workpieces. For metals, they involve plastic deformation of the workpiece, in which material is damaged below the tool and other material is moved onto the surface.

Theoretical methods to model these processes are available for all space and time scales of interest [1]. They range from continuum models of crystal plasticity over mesoscopic models—such as discrete dislocation dynamics or phase fields—to atomistic models based on molecular dynamics (MD).

The major advantage of MD is that all plastic processes as well as material damage are treated on a common basis, namely the interatomic interaction between the workpiece atoms. No further assumptions—such as on dislocation glide, reaction, or cross-slip—need to be introduced. However, the systems treated are of a size extending only over a few 10 nm and the transferability of the results to the micrometer scale and above needs to be validated by comparison to experiment. In addition,

H. M. Urbassek (✉) · I. Alabd Alhafez
Institute of Computational Material Science, RPTU Kaiserslautern, Kaiserslautern, Germany
e-mail: urbassek@rptu.de

H. Hasse · M. Kopnarski · S. Stephan
Institute of Engineering Thermodynamics, RPTU Kaiserslautern, Kaiserslautern, Germany
e-mail: simon.stephan@mv.uni-kl.de

M. Kopnarski
Institute of Surface and Thin Film Analytics (IFOS), Kaiserslautern, Germany

© The Author(s), under exclusive license to Springer Nature Switzerland AG 2024
J. C. Aurich and H. Hasse (eds.), *Component Surfaces*, Springer Series in Advanced Manufacturing, https://doi.org/10.1007/978-3-031-35575-2_3

simulated indent and scratch velocities are in the range of m/s such that movements over nanometers are achieved in times of nanoseconds, while in experiment velocities are several orders of magnitude smaller. This fact also affects the importance of thermally activated processes; these are as a rule suppressed in MD while they may contribute—due to the large timescales available—in microscopic experiments.

In many applications, the contact between tool and workpiece is not dry but lubricated. The effect of lubrication has not been studied as comprehensively as dry contacts, partly because the multitude of lubrication liquids available renders a generalized treatment difficult.

In this chapter, we present several novel insights obtained using MD for dry and lubricated indentation and scratching processes. In addition, selected experimental results are compared with these findings.

2 Simulation Method

In the present chapter, we focus on a workpiece consisting of elemental iron as a model of ferritic steels. The setup of the simulation system is shown schematically in Fig. 1. A block of crystalline bcc Fe is modeled atomistically; it is surrounded by layers in which a thermostat acts to keep the temperature at a constant value and outer layers where the atoms are fixed to prevent the workpiece from any translational movement during indentation and scratch. Often, simulations are performed at low temperature, <1 K, in order to ease the detection of crystal defects, in particular dislocations. Outside the workpiece, there may be vacuum or a lubricating fluid. Further information on the modeling of lubricated machining is provided in Sect. 4.

Fe atoms interact via a many-body potential of the embedded-atom-model type as detailed in Ref. [2]. Such many-body potentials allow to model the physics of metals—including defects, surfaces, and dislocations—realistically.

The tip is usually considered to be made of diamond and is often modeled as a sphere of radius R . Often, when the wear of the tip is not considered, the tip is considered to be rigid. This can be done by an atomistic sphere cut out from a block of diamond. The interaction between the C atoms of the tip and the Fe atoms of the workpiece is as a rule modeled by a purely repulsive potential; this can be simply chosen as a Lennard–Jones potential,

$$\Phi_{\text{LJ}}(r) = 4\epsilon \left[\left(\frac{\sigma}{r} \right)^{12} - \left(\frac{\sigma}{r} \right)^6 \right], \quad (1)$$

cut off at the potential minimum. Here, r denotes the distance between two atoms, ϵ is an energy parameter equal to the bond energy, and σ is a length parameter characterizing the distance where the potential energy vanishes.

An alternative approach [3] uses a non-atomistic tip, modeled as a repulsive sphere,

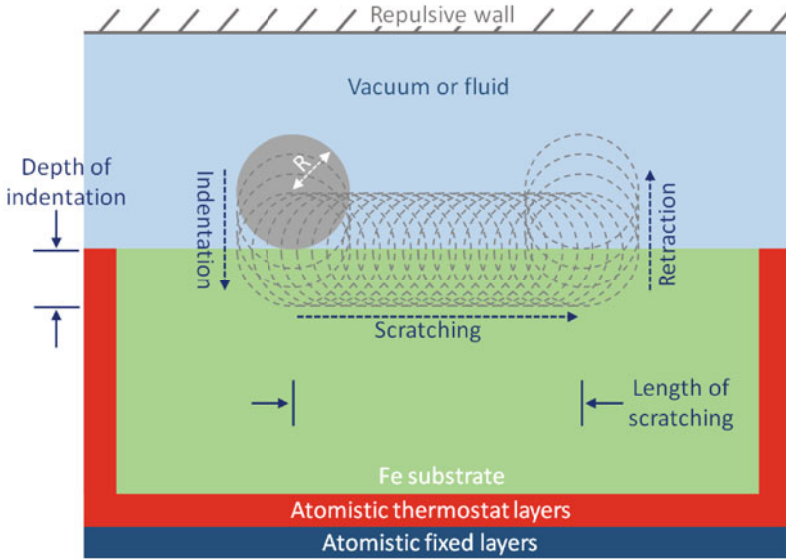


Fig. 1 Setup of the simulation system, illustrating the path of the tip during the processes of indentation, scratching, and retraction

$$V(r) = \begin{cases} k(R - r)^3, & r < R, \\ 0, & r \geq R, \end{cases} \quad (2)$$

where r is the distance of a substrate atom to the center of the indenter. The indenter stiffness has been set to $k = 10 \text{ eV/\AA}^3$. Such a smooth indenter is akin to the concept of a Hertzian indenter as it shows no friction nor roughness. Indentation is described faithfully by smooth indenters [4–6]; however, the roughness of atomistic indenters may influence the dislocation nucleation process.

The tip is initially positioned above the surface, immediately outside the C–Fe interaction. For the indentation simulation, the indenter moves into the substrate up to the final depth of $d = 4 \text{ nm}$. Then the tip moves parallel to the surface up to the total scratch length of $L = 15 \text{ nm}$ and is finally retracted. These steps are indicated in Fig. 1.

The open-source LAMMPS code [7] is used to perform the simulations, and the dislocation extraction algorithm [8] to identify the dislocations and to determine their Burgers vectors. The free software tool OVITO [9] is employed to visualize the atomistic configurations.

3 Dry Indentation and Scratching

3.1 Dislocations

The generation of dislocations is exemplified in Fig. 2. This simulation was run on a block of Fe with a (100) surface and consisting of 22.1×10^6 atoms. The scratch direction is along $[0\bar{1}\bar{1}]$. The final indentation depth amounts to $d = 4$ nm and the scratch length to $L = 15$ nm. The contact radius for full indentation is given by

$$a_c = \sqrt{R^2 - (R - d)^2} \quad (3)$$

and amounts to $a_c = 8$ nm. In all stages, the indenter velocity amounts to 20 m/s.

Dislocations with Burgers vector $\underline{b} = \frac{1}{2}\langle 111 \rangle$ and $\langle 100 \rangle$ are created, which form a dense network adhering to the indent pit. A detailed inspection shows that shear loops are generated in the region of highest shear stress under the indenter; these loops expand with leading dislocation lines of an edge character followed by trailing lines of a screw character. The trailing screw lines annihilate leading to a pinch-off of the shear loop and its emission as a prismatic loop [11], as displayed on the right-hand side of Figure 2b.

As this example shows, the plasticity developing under the tool can be divided into a *plastic zone* proper—consisting of dislocations adherent to the impact or scratch groove—and ejected loops. The ejected loops migrate in the stress field gradient away from the plastic zone but their later fate is not easily modeled by MD due to the boundaries existing in the simulation volume. Eventually, these loops will be pinned by some defects existing in the workpiece far from the indent zone. The plastic zone adherent to the impact pit is of highest interest, since it is this zone that will also be visible in actual microscopy images.

The size of the plastic zone, R_{pl} , may be defined as the largest distance of the adherent dislocations to the center of the contact zone [12, 13]. In experiment, R_{pl} is found to scale with the radius of the contact zone, a_c , Eq. (3), such that the plastic-zone size factor

$$f = \frac{R_{\text{pl}}}{a_c} \quad (4)$$

is of the order of $f = 2\text{--}3$ [14, 15]. MD simulations of nanoindentation in a variety of metals—with hcp, bcc, and fcc crystal structures—show that this behavior also applies to the nanoworld [12, 16].

3.2 Groove and Pile-up

After nanoindentation, the pile-up surrounding the indent pit shows the symmetry of the surface; this happens analogously for the pile-up structure of the scratch groove.

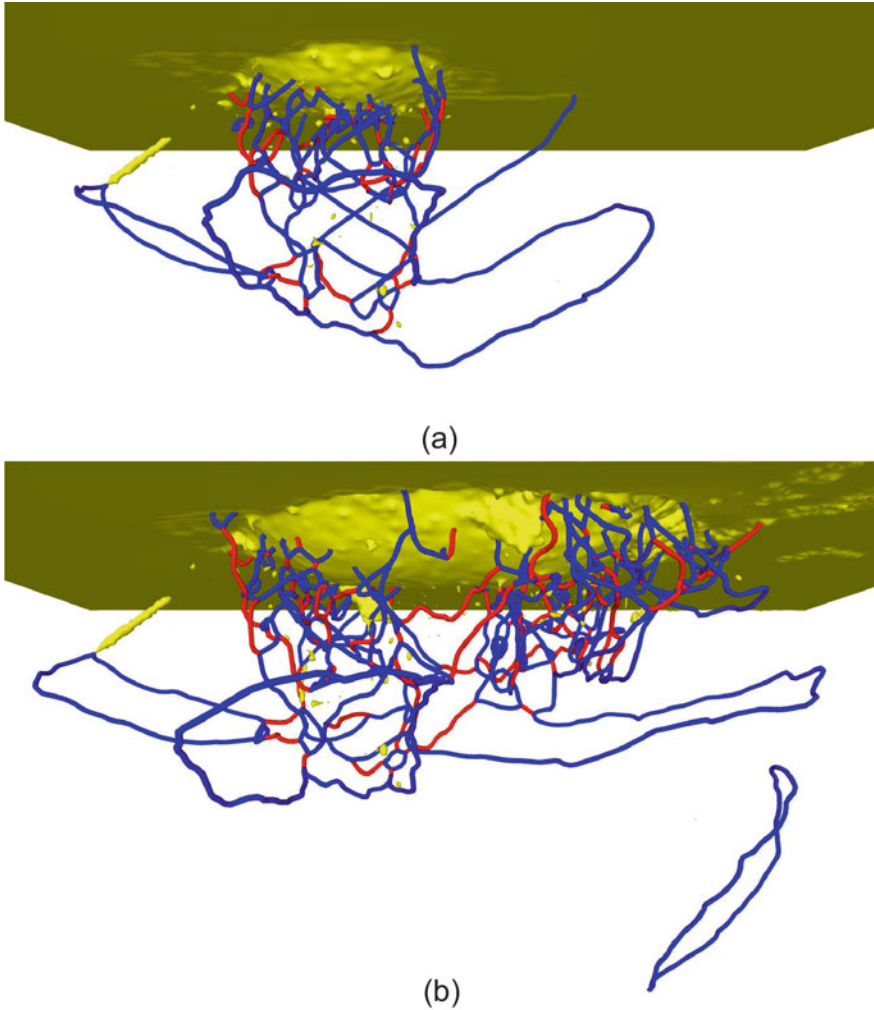


Fig. 2 Dislocation network developing **a** after indent and **b** after scratch. Dislocations are colored according to their Burgers vector b : blue $\frac{1}{2}(111)$ and red (100) . Yellow denotes the surface of the indent pit as well as unidentified defects. The snapshots are at the same scale. Data taken from Ref. [10] under CC BY 3.0

Figure 3 exemplifies this finding for scratching of the (100) , (110) , and (111) surfaces of Fe in several low-index directions. In this simulation, a small tip ($R = 2.1$ nm) was used and correspondingly the indent depth $d = 2.1$ nm and scratch length $L = 5$ nm could be chosen smaller than in the example shown above.

The structure of the pile-up is generated by the anisotropic slip occurring in crystals since pile-up is generated by atoms transported onto the surface along slip directions—identical to the Burgers vector of the relevant dislocation—on a slip

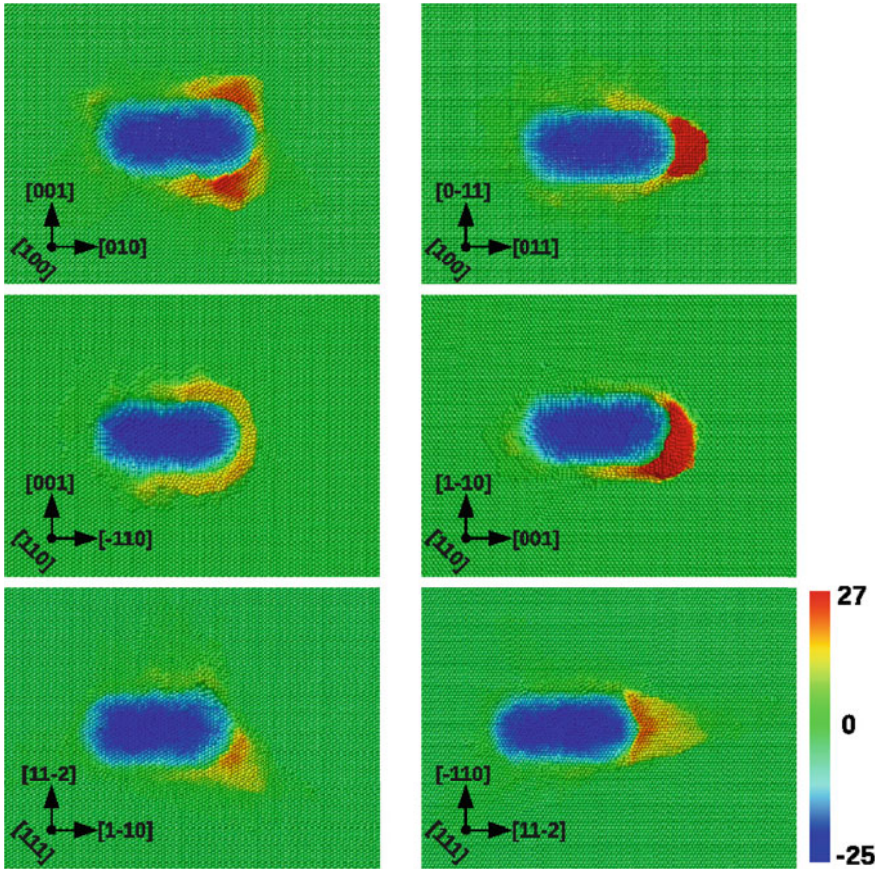


Fig. 3 Synopsis of pile-up formation after scratching and indenter retraction. Color codes height above the surface in Å. Taken with permission from Ref. [17]

plane. In the simplest picture, slip occurs in bcc Fe along the $\langle 111 \rangle$ directions. The relevant glide planes in Fe are the $\{110\}$ and $\{112\}$ planes.

Thus, we expect symmetric pile-ups for the (100) surface, which goes in an oblique direction sideways for scratch in [010] direction—along $[111]$ and $[1\bar{1}\bar{1}]$ —and is predominantly frontal for the [011] scratch direction (along $[111]$); this is corroborated by Fig. 3. A similar analysis gives a (more or less) symmetric pile-up for the (110) surface [17]. Most interesting is the scratch of the (111) surface as it has a three-fold symmetry. Here only scratch along $[11\bar{2}]$ leads to a symmetric pile-up as the relevant slip vector points along the scratch direction. Scratch in $[1\bar{1}\bar{0}]$ direction leads to asymmetric pile-up since only glide along $[11\bar{1}]$ leads to pile-up towards the front while the second activated slip system in $[11\bar{1}]$ direction assembles the pile-up on the lateral side of the groove.

3.3 Hardness and Friction

The determination of the forces acting on the tool is straightforward in an MD simulation; Fig. 4 a gives an example of the forces during scratching specified in Sect. 3.1, cf. Fig. 2. After indentation, the normal force decreases, since less force is required to keep the tip at constant depth d . Simultaneously, the transverse force increases as the tip starts digging its groove sideways. This *onset regime* has a length of 4 nm, roughly equivalent to the tip depth d . Later, the normal force saturates, while the transverse force steadily increases, as the pile-up in front of the tip keeps growing.

The friction coefficient, μ , is defined as the ratio of the transverse force, F_t , to the normal force, F_n ,

$$\mu = \frac{F_t}{F_n}. \tag{5}$$

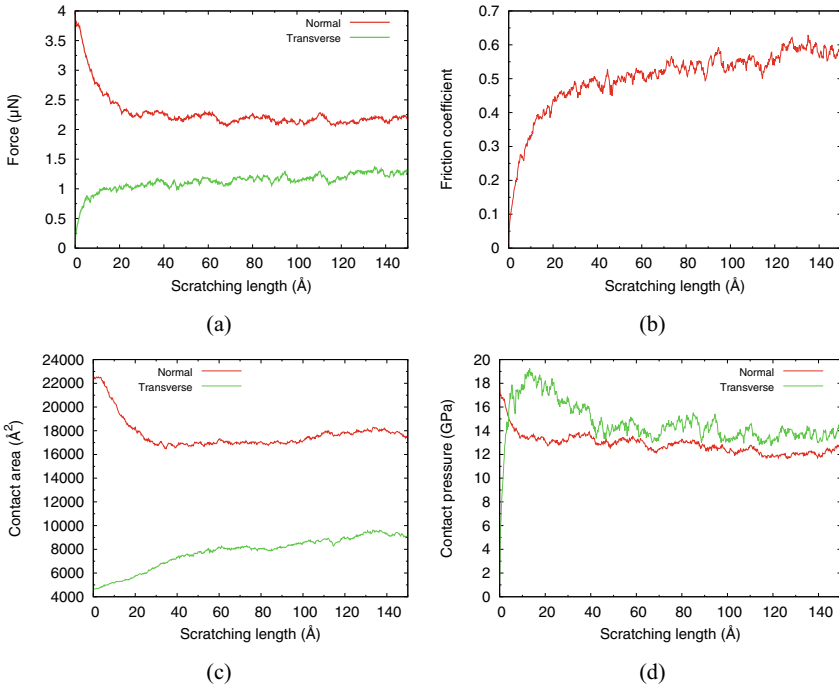


Fig. 4 **a** Forces, **b** friction coefficient, **c** contact areas, and **d** contact pressure during a scratch simulation. Data correspond to the simulation leading to the dislocation pattern in Fig. 2. Data taken from Ref. [10] under CC BY 3.0

It does not saturate, see Fig. 4 b, as the transverse force is constantly growing even after the end of the onset regime; this growth is caused by the constantly growing pile-up in front of the tool, cf. Fig. 3.

The calculation of the contact pressure,

$$p = \frac{F}{A}, \quad (6)$$

requires the determination of the contact area of the tip with the workpiece during the simulation. For the normal contact pressure, the force F_n is divided by the normal contact area, i.e., the projection of the contact area between the tip and the workpiece into the surface plane, $A_n = \pi a_c^2$, see Eq. 3. Analogously, a transverse contact pressure can be defined in which the transverse force is divided by the transverse area, A_t , which is the projection of the contact area between the tip and the workpiece into the plane orthogonal to the scratch direction. In experiments, the projection of the submerged part of the tip is used, while in MD, one may use the position of the atoms contacting the tip to determine these areas [17, 18]. Figure 4 c shows the evolution of these areas with scratch length; the normal area decreases after the onset regime as the rear part of the tip loses contact with the groove bottom, while the transverse area increases due to the growth of the frontal pile-up.

After the onset regime, the contact pressures assume roughly constant values, Fig. 4 d; these are denoted as the (normal or transverse) hardness of the material. Fluctuations occur since, in particular, the force is subject to fluctuations generated by the generation and emission of dislocations in the plastic zone. Such fluctuations will be smeared out for slower processes and larger indenters, i.e., in comparisons with larger-sized experiments. In nanoscopic simulations, hardness is not a material characteristic but depends on the process. Thus, it decreases with increasing indenter size [6] in agreement with the indentation size effect [19, 20] which originates in the decrease of dislocation density—and hence of Taylor hardening—for larger tips [19–21].

Assuming that normal and transverse hardnesses are approximately equal [22], the friction coefficient, Eq. 5, is simply given by the ratio of transverse and normal areas. Using the geometrical areas, this prediction gives a value of $\mu = 0.45$, in rough agreement with the simulation result immediately after the onset regime [10].

3.4 Tip Geometry

Actual tips used for indentation or scratch experiments often have a pyramidal—Berkovich or Vickers—form. However, on a nanoscale, they are rounded at their end, with curvature radii that may be as small as several ten nm. Thus, the simulations described above may be realistic for indentation and scratch depths in the nm range. Nonetheless, it is interesting to study the dependence of the indentation and scratch mechanisms on the shape of the indenter by scaling down the size of

actual indenters to the nanoscale. Such simulations have been performed for conical indenters, Berkovich pyramids, and cube-corner indenters [23, 24].

Figure 5 shows the dislocation network developing under a conical indenter after scratching in dependence of the semi-apex angle, β , of the cone. A strong increase of the network with β can be observed. It is related to the fact that the $\langle 111 \rangle$ slip directions form an angle of 54.7° to the surface normal. Hence, for large semi-apex angles, the cones obstruct slip to the surface leading to complex networks. In agreement with the increase of the dislocation network, also the indentation hardness increases with the semi-apex angle β , see Fig. 6a.

The friction coefficient shows a monotonically decreasing trend with β , Fig. 6b. This can be easily understood from a macroscopic argument. Assuming [22] that normal and tangential hardness during scratch are approximately identical, the friction coefficient, Eq. 5, is given by the ratio of transverse and normal areas, which can be calculated from geometry to give [23]

$$\mu = \frac{2}{\pi \tan \beta}. \quad (7)$$

The close agreement of this law with the MD simulations, Fig. 6b, shows that, in this case, macroscopic ideas on friction hold down to the nanoscale.

Simulations with spherical and pyramidal indenters can be compared to conical indenters using the concept of an *equivalent cone angle* [25]. It is defined by stipulating that the ratio of the normal contact area to the indentation depth d is identical to that of a cone. This gives an equivalent cone angle for the pyramid of $\beta_B = 70.3^\circ$. For a sphere, the equivalent angle depends on the indentation depth; in our case, it is equal to $\beta_s = 63.4^\circ$. Figure 6 exemplifies that this idea of an equivalent cone angle works well for the Berkovich pyramid, since this pyramid is a self-similar structure and β_B does not depend on indentation depth. For the sphere, this concept does not work so well; the sphere shows a smaller hardness and a higher friction coefficient than an equivalent cone. This deviation may be traced back [23] to the fact that the cone has an (atomically) sharp tip, while the sphere is blunt; for small indentations $d \ll R$, it actually appears flat. This finding demonstrates that blunt indenters exhibit a different scratching behavior than sharp indenters. Also, the onset of plasticity during indent occurs considerably later than for sharp indenters.

3.5 Multiple Indentation

Multiple (or cyclic) indentation into the same position on a workpiece has been employed to characterize cumulative plasticity in materials [26, 27]. The repeated indentation cycles are as a rule performed to the same maximum load. Since every indentation changes the state of defects—in particular, the dislocations—inside the material, repeated indentation cycles lead to different material responses.

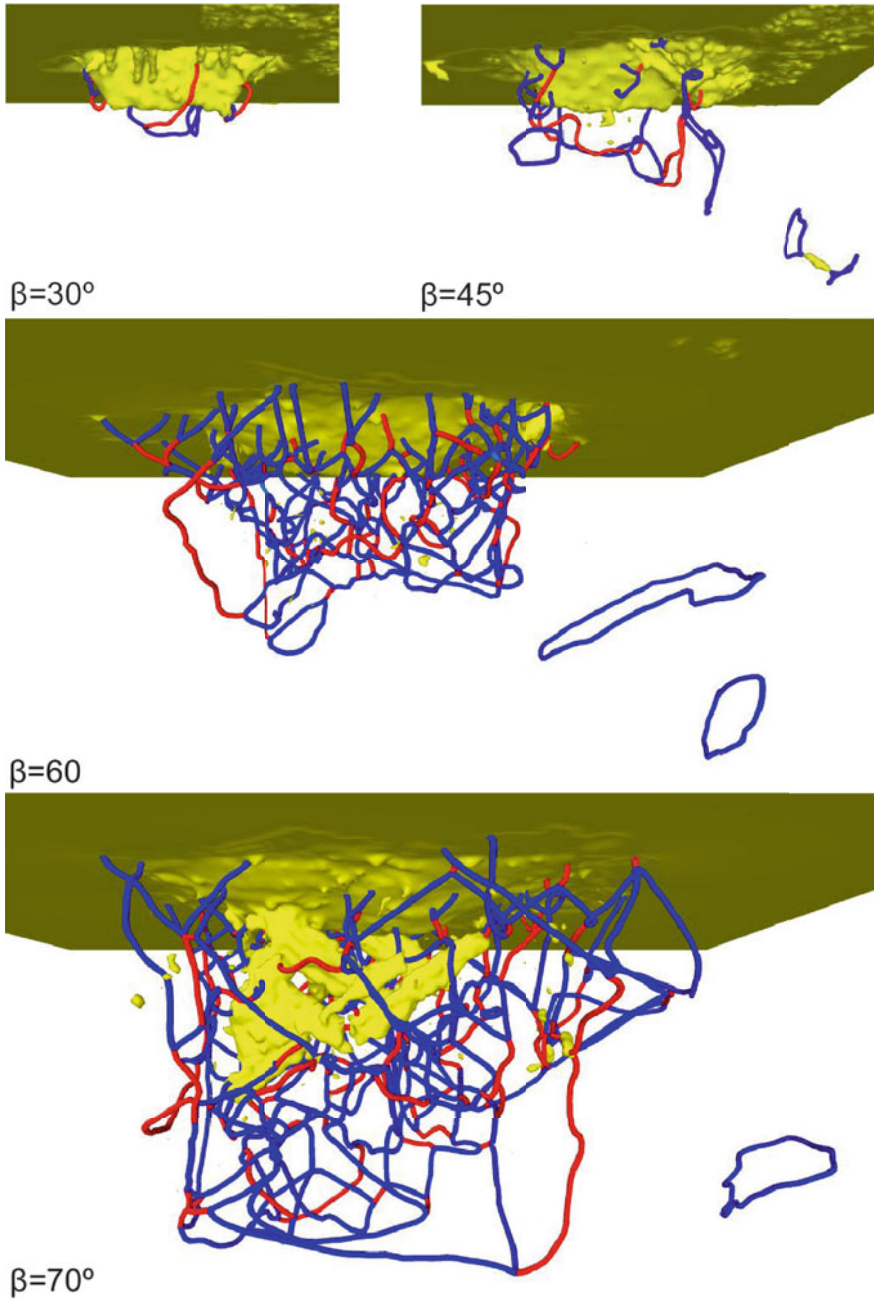


Fig. 5 Dislocation network generated after scratching and retraction of a conical tip with semi-apex angle β as indicated. Dislocations colored as in Fig. 2. The snapshots are at the same scale. Taken with permission from Ref. [23]

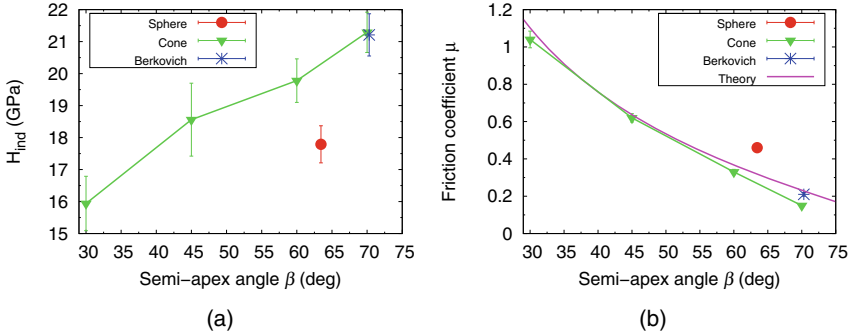


Fig. 6 Dependence of the **a** indentation hardness and **b** friction coefficient on the semi-apex angle β . A (100) Fe surface is scratched in the $[0\bar{1}\bar{1}]$ direction. Data for the spherical indenter and the Berkovich indenter are included at the respective equivalent cone angles. Lines are to guide the eye. The friction results denoted as “Theory” present Eq. 7. Taken with permission from Ref. [23]

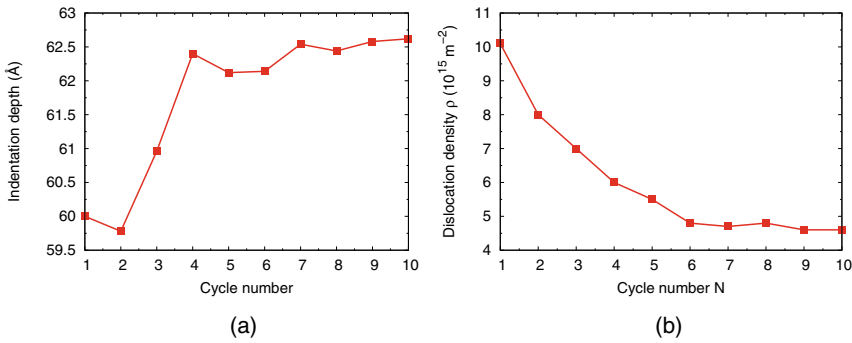


Fig. 7 Multiple indentation: Dependence of the **a** maximum indentation depth and **b** dislocation density in the plastic zone on cycle number. Taken from Ref. [26] under CC BY

Figure 7 illustrates this phenomenon, for example, of an Fe (100) surface. The first indentation—into a defect-free ideal crystal—was performed to a depth of 6 nm and required a maximum force of $4.55 \mu\text{N}$. Repeated indentations with the same maximum force allowed the indenter to penetrate deeper into the material, Fig. 7a. This indicates that the dislocation network generated by the first indent is further modified by subsequent indentations. A detailed inspection [26] of these changes shows that the total length of dislocations was reduced from $1.07 \mu\text{m}$ after the first indent to $0.69 \mu\text{m}$ after the tenth indent. Concomitantly, the size of the plastic zone grew from 36.2 to 40.4 nm. In total, the density of dislocations decreased in the plastic zone by a factor of around 2, see Fig. 7b. These changes reflect the relaxation of the dislocation network under the multiple plastic deformations occurring in a cyclic indentation scenario.

4 Lubrication

Lubrication plays an important role in tribological and machining processes. It serves twofold: On the one hand, lubrication reduces the friction and thus weakens the generation of heat in the contact process. On the other hand, the working fluid cools the solid bodies, acting as a heat sink. Both functionalities were investigated for a nanoscopic scratching process by means of molecular dynamics simulations.

The contact process depicted in Fig. 1 was adapted here using a fluid as lubricant. Two different situations were considered: (1) a simple, yet representative and generic model system [28–31]; (2) specific real substance systems [32, 33]. For the model system, a quasi-two-dimensional setup was used. Hence, the indenter was a cylinder. For the real substance systems, the indenter was a sphere [32] or a spherical cap [33]. As lubricant, in a first study, methane was used [32]; in a second study, both methane and decane were used [33]. The force fields of the real substance fluids, which we have also studied regarding bulk phase properties [34, 35], were taken from an extended version of the MolMod database [36].

Here, the focus is on the lubricated model systems. Results for the lubricated model system are presented and discussed using the Lennard–Jones units system (see Chap. 9 and Ref. [37] for details). The force field settings, simulation parameters, and simulation box configurations applied here were adopted from Refs. [29, 30].

For the model system, the Lennard–Jones truncated & shifted (LJTS) model potential was used for describing all applicable interactions. The LJTS model system has been extensively studied in the literature. Therefore, the relation of many macroscopic properties to the model parameters as well as the thermodynamic state point has been elucidated, e.g., for the vapor–liquid equilibrium [38, 39], the wetting behavior [40, 41], the transport properties [35, 42, 43], and interfacial properties [44, 45]. Details on the LJTS model system are discussed in Chap. 9. Here, the model system was in particular used to systematically study the influence of the solid–fluid interaction energy on the contact process properties.

Figure 8 shows the results for the coefficient of friction (COF) in the scratching process. In the starting phase of the scratching process, the COF is larger in the dry case. Vice versa, in the quasi-stationary phase, the COF is larger in the lubricated case. The presence of a lubricant reduces the COF by about 25% compared to the dry reference case, which is due to the fact that a significant amount of lubricant molecules remain between the indenter and the substrate in the starting phase until they are squeezed out of the gap between the indenter and the substrate. The presence of the lubricant molecules in the gap result in an increased normal force and a slightly decreased tangential force in the starting phase [29]. Once the fluid molecules are squeezed out and the contact is essentially dry with ongoing scratching, the coefficient of friction is increased by the presence of a fluid compared to a dry case by approximately 15%. This is due to the fact that individual fluid molecules are imprinted into the substrate surface, which requires additional work being done by the indenter [32]. The change in the COF by the presence of a fluid is practically independent of the energy of the solid–fluid interaction, cf. Fig. 8-right.

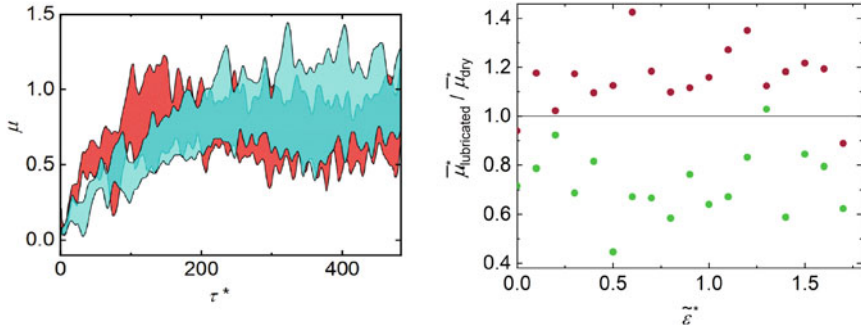


Fig. 8 Coefficient of friction sampled in dry and lubricated simulations. Left: COF as a function of the simulation time during the scratching process for a dry case (red) and a lubricated case (blue). The lubricated case had the solid–fluid interaction energy $\tilde{\epsilon}^* = 0.5$. The shaded areas (red and blue) are bands of the width of the standard deviation obtained from a set of eight simulation replicas around their arithmetic mean. Right: average COF as a function of the reduced solid–fluid interaction energy obtained in the starting phase (brown symbols) and a steady-state phase (green symbols). Data taken from Refs. [29, 30]

Figure 9 shows the temperature field (left) and the thermal balance (right) of the scratching process. For the temperature field, results for a dry case (top) and a lubricated case (bottom) are shown. For the thermal balance, ΔU_S^* and ΔU_F^* indicate the changes in the total energy (kinetic + potential energy) of the substrate and the fluid, respectively. $Q_{\text{thermostat}}^*$ is the total heat removed from the system by the thermostat and W_I^* is the work done by the indenter on the system. All properties of the energy balance W_I^* , ΔU_S^* , ΔU_F^* , and Q_{Th}^* are normalized at each time step during the simulation by the work done by the indenter at the end of the contact process $W_{\text{I,dry}}^*(\tau_{\text{end}}^*)$ in the dry case

$$\Delta E_{\text{norm}}(\tau^*) = \frac{Z(\tau^*)}{W_{\text{I,dry}}^*(\tau_{\text{end}}^*)} \quad \text{with } Z = W_I^*, \Delta U_S^*, \Delta U_F^*, Q_{\text{Th}}^*. \quad (8)$$

The presence of a fluid has a significant influence on the temperature field of the fluid and the energy balance of the process [29]. The fluid in the direct vicinity of the formed chip shows a significantly increased temperature compared to the bulk material, cf. Fig. 9-left. The temperature field moreover reveals that the temperature in the substrate decays much faster than in the fluid. This is due to the fact that the heat conductivity in the substrate is about an order of magnitude higher than that in the fluid. The maximum temperature is found at the tip of the chip.

The heat impact on the substrate is reduced up to 20% by the presence of a lubricant compared to a dry simulation, cf. Fig. 9-right. Two effects contribute to the cooling effect: (a) the fluid reduces the friction during the starting of the scratching and therefore reduces the amount of dissipated energy in the contact zone; (b) a heat flux from the contact zone to the fluid directly cools the contact zone. Moreover, the

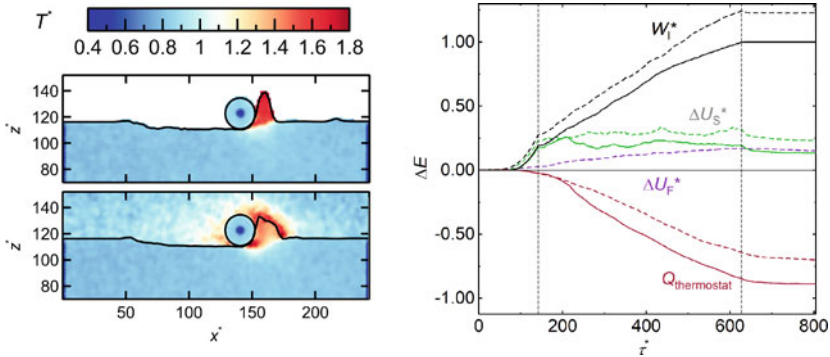


Fig. 9 Temperature field in the simulation box in lubricated simulation (left) for a dry case (top) and a lubricated case (bottom) and thermal balance as a function of the simulation time (right). The lubricated case had the solid–fluid interaction energy $\tilde{\epsilon}^* = 0.5$. For the temperature profiles (left), the temperature was averaged over the box length in y -direction. For the thermal balance, solid lines indicate a dry reference case and dashed curves indicate the lubricated case. Details are given in Ref. [29]. Data taken from Refs. [29, 31]

cooling capabilities of the fluid have been found to be dependent on the energy of the solid–fluid interaction, which has been discussed in detail by Stephan et al. [29].

The main part of the work done by the indenter is found to dissipate and is removed from the system via the substrate thermostat, cf. Fig. 9. The potential energy of the substrate fluctuates in the stationary phase of the scratching but does not steadily increase with the ongoing formation of the chip. The energy dissipation dominates the energy balance compared to the energy required for defect generation and plastic deformation.

By performing sets of replicas, the statistical uncertainties of the non-equilibrium MD simulation observables were estimated [30]. The standard deviation of a given observable of a set of replicas, which solely differ in the initial thermal motion is normalized for each observable so that the reliability of the findings derived from different properties can be compared. Most importantly, the statistical uncertainty of all investigated observables was found to quickly converge during the scratching process. Hence, differences among the simulations of a set of replicas do not build up with the simulation time.

5 Relation to Experimental Observations

5.1 Experimental

Experimental results related to the simulations are derived from indentation and scratch tests performed with a nominally conical diamond indenter on an Fe single

crystal surface. The standard indenter with an apex angle of 90° is rounded at its tip. According to the manufacturer's information, the radius of curvature is less than $1\ \mu\text{m}$. In this section, the focus of the investigations will be on scratch experiments in the $[0\bar{1}\bar{1}]$ direction of the (100) surface of the crystal. After the indenter has touched the surface, the load F_n is linearly increased up to a fixed value (indentation) and then moved parallel to the surface for the scratching experiments with an almost constant normal force and a constant speed of $0.1\ \mu\text{m/s}$ (scratching). The lateral force is measured over the scratch length of typically $5\ \mu\text{m}$, then the tip is pulled out of the surface and the topography of the scratch is measured with an atomic force microscope (AFM) in tapping mode (tip radius $< 10\ \text{nm}$). Loading and unloading times are both $15\ \text{s}$ for the scratching experiments, while the unloading times for the indentation experiments are only $5\ \text{s}$. Scratch and indentation tests were repeated between 5 and 15 times for each measured value and the results are averaged accordingly. In order to prevent small metal particles adhering to the indenter tip from influencing the results, the indenter was subjected to a special procedure before each series of measurements: In order to remove any metal particles adhering to the indenter tip, 10 indentations are carried out on a fused silica surface with almost the maximum permissible normal force. This procedure is repeated after each measurement series with a maximum of 10–12 scratches. Tests with the smallest and largest loads are carried out twice, at the beginning and at the end of a series. Since there was no significant difference between the results, it is assumed that these were not influenced by adhering metal particles.

5.2 Groove, Pile-up, and Tip Geometry

Figure 10 on the left shows AFM results after an indentation measurement with a load of $F_n = 300\ \mu\text{N}$; on the right, the corresponding 3D representation for the scratched surface is shown. Due to the four $\langle 111 \rangle$ slip directions available in an intact crystal (cf. Sect. 3.2), one expects a four-fold symmetry for material ejection beside the indentation. While the four-fold symmetry is clearly evident for larger loads, due to contaminations and irregularities on the Fe surface, the full four-fold symmetry could not always be observed for $F_n < 500\ \mu\text{N}$. As observed in the simulation (see Fig. 3-top right), for the scratch experiments the pile-up should appear predominantly in the forward direction in front of the scratch. In contrast, the experiments for low loads ($< 300\ \mu\text{N}$) show the ejected material almost exclusively sideways along the scratch track (Fig. 10-right). A possible explanation for this behavior is that during scratching the material originally excavated in front of the indenter tip is transported sideways along the indenter surface, at least for scratch lengths that are significantly longer than in the simulation. Another explanation could also be the effect of so-called subsurface lattice rotations [46], which under certain conditions can reduce long-range stress fields. Since such effects would be relatively slow on the one hand and wide-ranging on the other, it is not expected that they would be noticeable in the MD simulation, but could play a role in the experiment.

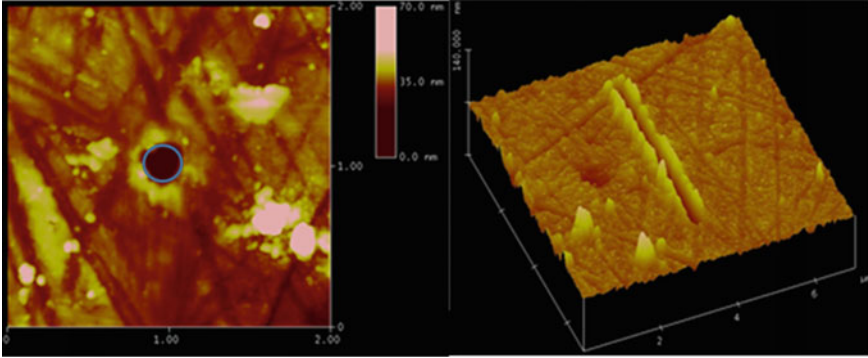


Fig. 10 Two-dimensional representation of an indent on an Fe (100) surface taken at a normal force of $300 \mu\text{N}$ (left side); three-dimensional representation of a scratch in the $[0\bar{1}1]$ direction with the same normal force value (right side)

Since the penetration depth is small enough for low loads, the indentation image can be used to obtain information about the actual radius of curvature at the tip of the indenter. The radius of the circle drawn in Fig. 10 is $a \approx 110 \text{ nm}$, and accordingly, the indentation depth is $d \approx 27 \text{ nm}$. If the shape of the indenter tip for this is still small, the depth d is completely approximated by a sphere and the radius obtained is $R = (a^2 + d^2)/(2d) \approx 240 \text{ nm}$. Hence, the indenter used here can be described by a cone (semi-apex angle $\beta = 45^\circ$) with a sphere of radius R at the tip, the slope of which is chosen also to be β at the transition to the cone.

5.3 Friction and Hardness

As in the simulation, the forces exerted during scratching can be measured relatively easily both in the lateral and in the normal direction, i.e., F_t and F_n , so that the coefficient of friction μ is calculated using Eq. 5. Figure 11 shows on the left experimentally determined coefficients of friction plotted over the length of the scratch, and on the right, results from the simulation [17]. The corresponding loads F_n and the corresponding scratch depth values are also included. The experimental curves represent mean values of relatively large areas and over many individual measurements (5–15) and show therefore a significantly smoother course compared to the friction values obtained from the simulation. In the simulated curves, the onset range of the friction values can be assigned approximately to the radius of the indenter tip (here R is always 2.14 nm), in the experimental curves, it is correlated with the radius of the associated indentation. After that, the coefficients of friction in both cases reach more or less constant values that depend on the respective indentation depth. The reason for this behavior is that the projected tangential submersed indenter area A_t for non-self-similar indenter geometries does not remain constant in relation to the

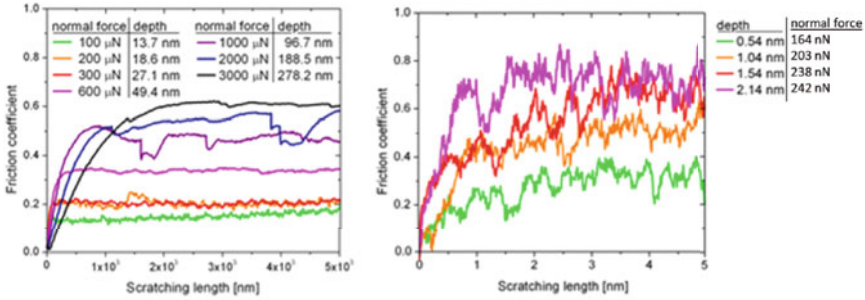


Fig. 11 Evolution of the friction coefficient during scratching of an Fe (100) surface in the $[0\bar{1}\bar{1}]$ direction for various normal loads. The associated penetration depths are also given; experimental data (left side) and simulation results (right side) [17]

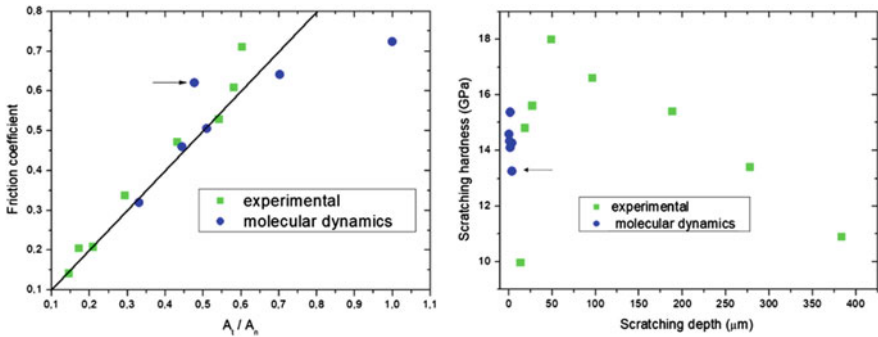


Fig. 12 Comparison of experimental results on friction coefficients (left side) and normal hardness values to molecular dynamic calculations (data from Refs. [17, 23]). The scratch tests were carried out experimentally with a cono-spherical indenter. The molecular dynamic data mainly belong to simulations with a spherical indenter. Results for a conical indenter (same semi-apex angle as in the experiment) are indicated by an arrow. All data are for the same Fe substrate surface and scratching direction as described in the text

normal contact area A_n ; the ratio increases with increasing indentation depth [23]. This can be clearly seen in Fig. 12-left, where experimental and simulated coefficients of friction are plotted against the associated ratio A_t/A_n . Here, A_n is always half of the cross-sectional area of the indenter, since the rear part of the indenter has lost contact with the scratch groove. The plot shows that the measured and simulated coefficients of friction are in good agreement with the theory of Bowden and Tabor [22], which assumes no difference between the scratch hardness in the tangential and normal direction, H_t or H_n respectively, so that μ is determined exclusively by the geometric ratio A_t/A_n . Deviations from this behavior are only indicated for area ratios above 0.5.

For the explicit measurement of the associated hardnesses $H_t = F_t/A_t$ and $H_n = F_n/A_n$, in addition to the forces, the actual respective contact areas A_t and A_n must also be determined. A precise measurement of these areas, which goes

beyond an estimation of the areas alone from the geometric shape of the indenter, as described above, turns out to be particularly difficult both in the simulations and in the experiment. While the actual contact areas cannot be observed in situ during scratching in the experiments, this can still be done in the simulations by determining the contact area occupied by the indenter's contacting substrate atoms [17]. For measuring the associated contact pressures, however, the load transferred with each element of contact area and the role of the resulting pile-up would also have to be taken into account. Figure 12-right shows the progression of the scratch hardness H_n over the respective penetration depth. In the case of the experimental values, the areas A_n are determined from the geometry of the indenter tip, while these were explicitly evaluated in the simulations. In the area of small penetration depths, there is a fair agreement between the molecular dynamic calculations and the experimental values. For greater penetration depths, a drop in hardness values can be observed. This general trend, which is also reflected in the indentation hardnesses, is caused by the indentation size effect [46] which leads to strain hardening of the material with increasing dislocation densities (small penetration depths).

6 Relation to Friction on a Macroscopic Scale

In contrast to the one-time stress on the metal surface in the nanoscratch experiment, a pronounced running-in behavior must be taken into account in the case of recurring stress in a laboratory tribometer used in practice. Here, the metal surface to be tested is moved back and forth on a straight, 10 mm long line segment under a fixed diamond Vickers tip with a maximum relative speed of 10 mm/s. The normal force F_n exerted during the linear reciprocating movement is $F_n = 5$ N. Note that nominally sharp-edged asperity forms, such as the intrinsically self-similar Vickers pyramid, generally have a non-zero radius of curvature at the apex. Even originally sharp-edged asperity profiles can be rounded off by the continued stress when scratching. In practice, the more spherical, i.e., not self-similar, shape of the asperity tip is the rule and decisive for the observed coefficient of friction. In Fig. 13 on the right, experimentally in a laboratory tribometer determined friction coefficient curves for two different orientations of the Vickers tip are distinguished in a double-logarithmic representation, depending on whether the pyramid's "edge" or its "plane" is aligned in the direction of the scratch. It turns out that at the beginning of the experiments, contrary to what is expected for a Vickers pyramid, an influence of the orientation of the Vickers pyramid relative to the direction of the scratch is actually not recognizable. On the other hand, one does find a difference in the coefficients of friction for the two materials used, which in turn is not to be expected for the self-similar shape of a Vickers pyramid. However, both experimentally observed findings are a consequence of the spherical shape of the outermost indenter tip when the scratching tests are carried out with the same normal force on steel samples of different hardness, i.e., case hardening steel 16MnCr5 and an austenitic TWIP steel (HSD600, see Chap. 12), and therefore different penetration depths have to be taken into account. Measuring

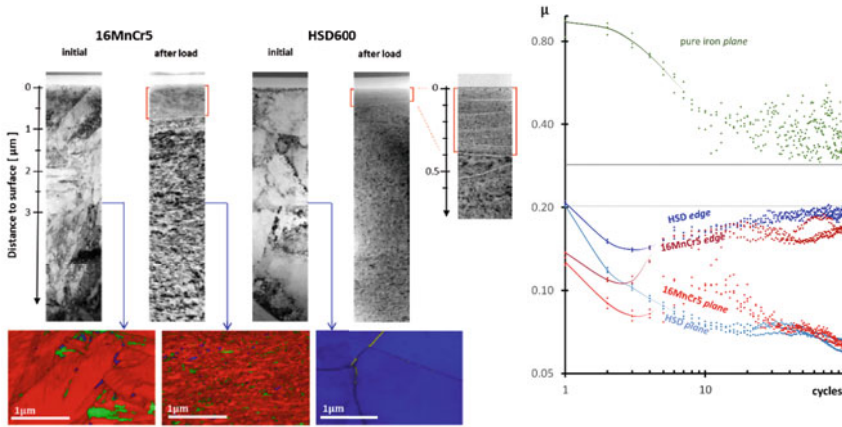


Fig. 13 Surface morphology (left side) and friction coefficient curves (right side) for a case-hardened steel (16MnCr5) and an austenitic HSD steel. Left: EFTEM brightfield and ACOM (Automated Crystal Orientation Mapping) images of cross-sectional areas near the surface, without and after tribological loading with $F_n = 5$ N, Vickers diamond, α -martensite (red), ϵ -martensite (yellow), austenite (blue), and ϵ -carbide phases (green). Right: development of the coefficient of friction for different materials as a function of the number of cycles

the tip profile in an electron microscope results in a value of around $R \leq 50 \mu\text{m}$ for its radius of curvature. With a microhardness that is above 700 HV for the case-hardened steel in the initial state and less than half this value for the HSD steel, the geometric approximation already described in this chapter actually gives friction coefficients μ_{geo} for the spherical indenter tip that is close to the measured values for both steels.

Due to characteristic changes in the morphology of the near-surface areas, the coefficient of friction can change significantly after repeated stress caused by repeated scratching of the same surface area. After about 100 load changes in the tribometer, the coefficients of friction for the two materials can hardly be distinguished, as was the case at the beginning of the tests. However, significant different μ values are now measured depending on the orientation of the Vickers tip. In order to be able to understand the similar values of the friction coefficients for different kinds of steel, the near-surface area in the scratch mark was analyzed in detail using EFTEM (Energy Filtered Transmission Electron Microscopy) (Fig. 13-left). For this purpose, the tests were selected with the pyramid surfaces oriented in the direction of the scratch and the associated cross-sectional lamellae were taken from the bottom of the wear track in a FIB (Focused Ion Beam).

Through the combined application of different analytical techniques, i.e., Selected Area Diffraction (SAD), Electron Precession Diffraction (PED), Energy-Dispersive X-ray spectroscopy (EDX), and Electron Energy Loss Spectroscopy (EELS), it becomes apparent [47] that two structurally clearly distinguishable tribolayers are formed in the 16MnCr5 steel, a fine-grained lower layer mainly of α -iron and a thin,

clearly separated and approximately $0.7\ \mu\text{m}$ thick, nanocrystalline layer above it (see red marking in Fig. 13-left) with additional small magnetite (Fe_3O_4) quantities. Like the unstressed base material, both layers have a high martensite content. In the case of the HSD steel, a very fine-grained area that reaches several micrometers into the structure and, clearly separated, a somewhat thinner, nanocrystalline zone of $0.4\text{--}0.6\ \mu\text{m}$ is created by grain refinement under tribological stress. The selected area diffraction proves that the predominantly austenitic starting material is almost completely transformed into α -martensite, while a mixture of the austenitic starting phase and the transition phase ϵ -martensite is still found in the fine crystalline zone below (see also Chap. 12). The chemical and structural properties of the near-surface zones of both materials, although clearly different in the initial state, have apparently become much more similar due to tribological stress [47].

As a result of the tribo-induced processes during many friction cycles, a similar nanocrystalline morphology appears in both materials, which offers comparatively less resistance to the lateral movement of the indenter on a solidified, fine-grained base material. With the pyramid orientation of the surface moving in the direction of the scratch, this leads obviously to a decrease in the coefficient of friction down to a value of $\mu = 0.06$, which is the same for both materials. Apparently, a different course is obtained if the Vickers orientation is chosen with the edge first. This probably results in other tribological properties in the relevant surface zone, which lead to different coefficients of friction for the edge orientation compared to the face orientation.

In Fig. 13-right, the course of the coefficients of friction for tests with the Vickers indenter on pure Fe (Fe99) is also given. Since the hardness of pure iron is only around 10% of that of case-hardening steel, the indenter now penetrates so deeply that the tip rounding described above is practically irrelevant. But μ is now even significantly higher than the area ratios calculated from the geometry of a Vickers indenter. The reasons for this are, as the comparatively “noisy” progression of the coefficients of friction indicates, adhesion processes that can be attributed to the known affinity of diamond to iron, as well as the significantly larger contact surface for pure Fe. Only with an increasing number of cycles do oxidation processes in particular [48] ensure that the influence of adhesion decreases again. In practice, the adhesion and affinity of the indenter material to the substrate material can indeed play a dominant role. This is shown, for example, in Fig. 14. An adhesive interaction or even the formation of chemical bonds between the indenter and the carrier material can only be avoided if the experiments are carried out with sufficient humidity so that the pure plowing part of the friction values can be observed. With steel instead of diamond, adhesion effects generally even gain in influence and μ depends strongly on air humidity, surface cleanliness [49] and wetting behavior [50].

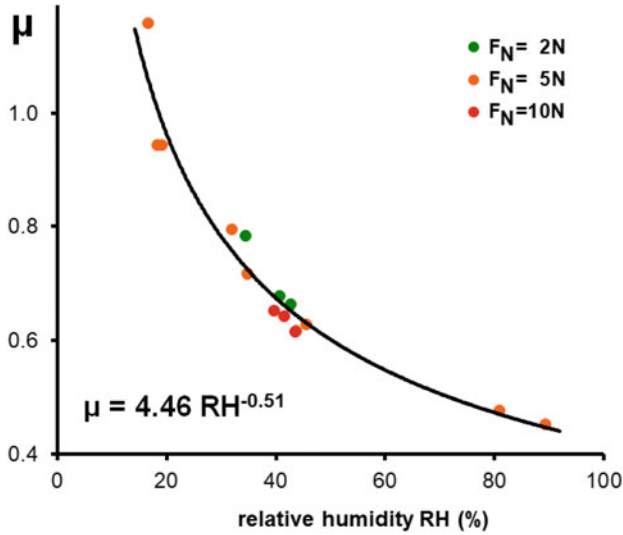


Fig. 14 Coefficient of friction μ as a function of the relative humidity RH for various loads ($F_n = 2, 5,$ and 10 N): The solid line corresponds to a simple exponential dependence $\mu(RH) = 4.46 RH^{-0.51}$. Only for $RH \geq 90\%$, friction is dominated by plowing

7 Summary

MD simulations of indentation and scratching allow to assess the atomistic processes occurring during the plastic deformation of materials. The present review highlighted several of the important findings as follows.

1. The size, R_{pl} , of the plastic zone adherent to the indent pit scales with the radius a_c of the contact zone, $R_{pl} = f a_c$. The plastic-zone size factor f assumes values of the order of 2–3, in agreement with experiments on the microscale.
2. Indentation and scratching of single crystals lead to anisotropic pile-up patterns. The distribution of the pile-up can be understood from a consideration of the activated slip systems that transport atoms onto the surface.
3. The determination of the material hardness requires an assessment of the contact area of the tool with the workpiece. During scratch, this contact area deviates from macroscopic considerations, in particular, because the pile-up generated in front of the scratch tip needs to be taken into account.
4. The friction coefficient during scratch follows the ratio of the transverse to normal contact areas as long as the frontal pile-up is negligible.
5. Tip geometry strongly influences the dislocations generated under the indenter and consequently hardness and friction coefficient. For sharp conical tips, the hardness increases and the friction coefficient decreases with a semi-apex angle.
6. Pyramidal tips follow the behavior of the cones if the pyramid is assigned its equivalent cone angle. Spherical tips behave differently as their shape is not self-

similar; this shows that blunt tips exhibit a different scratching behavior than sharp tips.

7. Multiple or cyclic indentation allows to assess the changes in the dislocation network under the multiple deformations.
8. For lubricated scratching, the coefficient of friction is increased compared to a dry case at the beginning of the scratching process when fluid particles remain in the gap. With ongoing scratching, the fluid particles are squeezed out of the gap and the contact becomes essentially dry. During that phase, the coefficient of friction in a lubricated case is slightly increased compared to a dry case, which is due to the fact that individual fluid particles are imprinted into the substrate surface.
9. The presence of a lubricant has important consequences for the thermal balance of a scratching process, i.e., it reduces the maximum temperature of the substrate and the heat flux into the substrate.

When comparing to experimental data, we find surprisingly good agreement with the calculated friction and hardness data provided by MD calculations. In particular, both MD and experiment find that the hardness on a nanoscale is higher than on a micro- or macroscale. This phenomenon is caused by the indentation size effect which is based on the decrease of dislocation density with tip size. Even in cases, where quantitative deviations occur between simulated and experimentally determined values, atomistic simulations prove to be useful for the interpretation of both individual effects and general trends. Such deviations may be caused not only by the different length and time scales used in the simulations but also by surface contaminations that may occur in experiment, as discussed in Sect. 6.

References

1. Raabe D (1998) Computational materials science. Wiley-VCH, Weinheim
2. Mendeleev MI, Han S, Srolovitz DJ, Ackland GJ, Sun DY, Asta M (2003) Development of new interatomic potentials appropriate for crystalline and liquid iron. *Philos Mag* 83:3977–3994. <https://doi.org/10.1080/14786430310001613264>
3. Kelchner CL, Plimpton SJ, Hamilton JC (1998) Dislocation nucleation and defect structure during surface indentation. *Phys Rev B* 58:11085–11088. <https://doi.org/10.1103/PhysRevB.58.11085>
4. Wagner RJ, Ma L, Tavazza F, Levine LE (2008) Dislocation nucleation during nanoindentation of aluminum. *J Appl Phys* 104:114311. <https://doi.org/10.1063/1.3021305>
5. Luan B, Robbins MO (2005) The breakdown of continuum models for mechanical contacts. *Nature* 435:929. <https://doi.org/10.1038/nature03700>
6. Ruestes CJ, Bringa EM, Gao Y, Urbassek HM (2017) Molecular dynamics modeling of nanoindentation. In: Tiwari A, Natarajan S (eds) *Applied nanoindentation in advanced materials*. Chapter 14. Wiley, Chichester, UK, pp 313–345. <https://doi.org/10.1002/9781119084501.ch14>
7. Plimpton S (1995) Fast parallel algorithms for short-range molecular dynamics. *J Comput Phys* 117, pp 1–19. <http://lammmps.sandia.gov/>, <https://doi.org/10.1006/jcph.1995.1039>
8. Stukowski A, Albe K (2010) Extracting dislocations and non-dislocation crystal defects from atomistic simulation data. *Model Simul Mater Sci Eng* 18:085001. <https://doi.org/10.1088/0965-0393/18/8/085001>

9. Stukowski A (2010) Visualization and analysis of atomistic simulation data with OVITO—the Open Visualization Tool. *Model Simul Mater Sci Eng* 18:015012. <http://www.ovito.org/>, <https://doi.org/10.1088/0965-0393/18/1/015012>
10. Alabd Alhafez I, Urbassek HM (2019) Influence of tip adhesion on nanoindentation and scratching. *Model Simul Mater Sci Eng* 27(6):065014. <https://doi.org/10.1088/1361-651x/ab27ed>
11. Remington TP, Ruestes CJ, Bringa EM, Remington BA, Lu CH, Kad B, Meyers MA (2014) Plastic deformation in nanoindentation of tantalum: a new mechanism for prismatic loop formation. *Acta Mater* 78:378–393. <https://doi.org/10.1016/j.actamat.2014.06.058>
12. Gao Y, Ruestes CJ, Tramontina DR, Urbassek HM (2015) Comparative simulation study of the structure of the plastic zone produced by nanoindentation. *J Mech Phys Sol* 75:58–75. <https://doi.org/10.1016/j.jmps.2014.11.005>
13. Alabd Alhafez I, Ruestes CJ, Urbassek HM (2018) Size of the plastic zone produced by nanoscratching. *Tribol Lett* 66(1):20. <https://doi.org/10.1007/s11249-017-0967-9>
14. Johnson KL (1985) *Contact mechanics*. Cambridge University Press, Cambridge
15. Durst K, Backes B, Göken M (2005) Indentation size effect in metallic materials: correcting for the size of the plastic zone. *Scr Mater* 52:1093–1097. <https://doi.org/10.1016/j.scriptamat.2005.02.009>
16. Alabd Alhafez I, Ruestes CJ, Gao Y, Urbassek HM (2016) Nanoindentation of hcp metals: a comparative simulation study of the evolution of dislocation networks. *Nanotechnology* 27(4):045706. <https://doi.org/10.1088/0957-4484/27/4/045706>
17. Gao Y, Brodyanski A, Kopnarski M, Urbassek HM (2015) Nanoscratching of iron: a molecular dynamics study of the influence of surface orientation and scratching direction. *Comput Mater Sci* 103:77–89. <https://doi.org/10.1016/j.commatsci.2015.03.011>
18. Ziegenhain G, Urbassek HM, Hartmaier A (2010) Influence of crystal anisotropy on elastic deformation and onset of plasticity in nanoindentation: a simulational study. *J Appl Phys* 107:061807. <https://doi.org/10.1063/1.3340523>
19. Nix WD, Gao H (1998) Indentation size effects in crystalline materials: a law for strain gradient plasticity. *J Mech Phys Sol* 46:411. [https://doi.org/10.1016/S0022-5096\(97\)00086-0](https://doi.org/10.1016/S0022-5096(97)00086-0)
20. Swadener JG, George EP, Pharr GM (2002) The correlation of the indentation size effect measured with indenters of various shapes. *J Mech Phys Sol* 50:681. [https://doi.org/10.1016/S0022-5096\(01\)00103-X](https://doi.org/10.1016/S0022-5096(01)00103-X)
21. Al-Rub RKA, Voyiadjis GZ (2004) Analytical and experimental determination of the material intrinsic length scale of strain gradient plasticity theory from micro- and nano-indentation experiments. *Int J Plast* 20(6):1139–1182. <https://doi.org/10.1016/j.ijplas.2003.10.007>
22. Bowden FP, Tabor D (1966) Friction, lubrication and wear: a survey of work during the last decade. *Brit J Appl Phys* 17:1521–1544. <https://doi.org/10.1088/0508-3443/17/12/301>
23. Alabd Alhafez I, Brodyanski A, Kopnarski M, Urbassek HM (2017) Influence of tip geometry on nanoscratching. *Tribol Lett* 65:26. <https://doi.org/10.1007/s11249-016-0804-6>
24. Zonana MC, Ruestes CJ, Bringa EM, Urbassek HM (2020) Effect of tip roundness on the nanoindentation of Fe crystals. *Tribol Lett* 68(2):56. <https://doi.org/10.1007/s11249-020-01295-9>
25. Fischer-Cripps AC (2004) *Nanoindentation*, 2nd edn. Springer, New York
26. Deldar S, Alabd Alhafez I, Smaga M, Beck T, Urbassek HM (2019) Cyclic indentation of iron: a comparison of experimental and atomistic simulations. *Metals* 9(5):541. <https://doi.org/10.3390/met9050541>
27. Chicot D, Roudet F, Zaoui A, Louis G, Lepingle V (2010) Influence of visco-elasto-plastic properties of magnetite on the elastic modulus: multi cyclic indentation and theoretical studies. *Mater Chem Phys* 119(1):75–81. <https://doi.org/10.1016/j.matchemphys.2009.07.033>
28. Lautenschlaeger MP, Stephan S, Urbassek HM, Kirsch B, Aurich JC, Horsch MT, Hasse H (2017) Effects of lubrication on the friction in nanometric machining processes: a molecular dynamics approach. *Appl Mech Mater* 869:85–93. <https://doi.org/10.4028/www.scientific.net/AMM.869.85>
29. Stephan S, Dya M, Urbassek HM, Hasse H (2019) The influence of lubrication and the solid-fluid interaction on thermodynamic properties in a nanoscopic scratching process. *Langmuir* 35(51):16948–16960. <https://doi.org/10.1021/acs.langmuir.9b01033>

30. Stephan S, Dyga M, Alabd Alhafez I, Urbassek HM, Hasse H (2021) Reproducibility of atomistic friction computer experiments: a molecular dynamics simulation study. *Mol Simul* 47(18):1509–1521. <https://doi.org/10.1080/08927022.2021.1987430>
31. Schmitt S, Stephan S, Kirsch B, Aurich JC, Kerscher E, Urbassek HM, Hasse H (2021) Molecular simulation study on the influence of the scratching velocity on nanoscopic contact processes. In: Garth C, Aurich JC, Linke B, Müller R, Ravani B, Weber GH, Kirsch B (eds) 2nd international conference on physical modeling for virtual manufacturing (iPMVM 2020), vol 89. Open Access Series in Informatics (OASISs). Schloss Dagstuhl - Leibniz-Zentrum für Informatik, Dagstuhl, Germany, pp 17:1–17:16. <https://doi.org/10.4230/OASISs.iPMVM.2020.17>
32. Stephan S, Lautenschlaeger MP, Alabd Alhafez I, Horsch MT, Urbassek HM, Hasse H (2018) Molecular dynamics simulation study of mechanical effects of lubrication on a nanoscale contact process. *Tribol Lett* 66(4):126. <https://doi.org/10.1007/s11249-018-1076-0>
33. Stephan S, Schmitt S, Hasse H, Urbassek HM (2023) Molecular dynamics simulation of the Stribeck curve: boundary lubrication, mixedlubrication, and hydrodynamic lubrication on the atomistic level. In: *Friction* (2023). in press
34. Schmitt S, Fleckenstein F, Hasse H, Stephan S (2023) Comparison of force fields for the prediction of thermophysical properties of long linear and branched alkanes. *J Phys Chem B* 127(8):1789–1802. <https://doi.org/10.1021/acs.jpcc.2c07997>
35. Fertig D, Hasse H, Stephan S (2022) Transport properties of binary Lennard-Jones mixtures: insights from entropy scaling and conformal solution theory. *J Mol Liq* 367:120401. <https://doi.org/10.1016/j.molliq.2022.120401>
36. Stephan S, Horsch M, Vrabec J, Hasse H (2019) MolMod-an open access database of force fields for molecular simulations of fluids. *Mol Simul* 45(10):806–814. <https://doi.org/10.1080/08927022.2019.1601191>
37. Stephan S, Thol M, Vrabec J, Hasse H (2019) Thermophysical properties of the Lennard-Jones fluid: database and data assessment. *J Chem Inf Model* 59(10):4248–4265. <https://doi.org/10.1021/acs.jcim.9b00620>
38. Vrabec J, Kedia GK, Fuchs G, Hasse H (2006) Comprehensive study of the vapour-liquid coexistence of the truncated and shifted Lennard-Jones fluid including planar and spherical interface properties. *Mol Phys* 104(9):1509. <https://doi.org/10.1080/00268970600556774>
39. Stephan S, Liu J, Langenbach K, Chapman WG, Hasse H (2018) Vapor-liquid interface of the Lennard-Jones truncated and shifted fluid: comparison of molecular simulation, density gradient theory, and density functional theory. *J Phys Chem C* 122(43):24705–24715. <https://doi.org/10.1021/acs.jpcc.8b06332>
40. Becker S, Urbassek HM, Horsch M, Hasse H (2014) Contact angle of sessile drops in Lennard-Jones systems. *Langmuir* 30(45):13606. <https://doi.org/10.1021/la503974z>
41. Heier M, Stephan S, Diewald F, Müller R, Langenbach K, Hasse H (2021) Molecular dynamics study of wetting and adsorption of binary mixtures of the Lennard-Jones truncated and shifted fluid on a planar wall. *Langmuir* 37:7405–7419. <https://doi.org/10.1021/acs.langmuir.1c00780>
42. Diewald F, Lautenschlaeger M, Stephan S, Langenbach K, Kuhn C, Seckler S, Bungartz H-J, Hasse H, Müller R (2020) Molecular dynamics and phase field simulations of droplets on surfaces with wettability gradient. *Comput Methods Appl Mech Eng* 361:112773. <https://doi.org/10.1016/j.cma.2019.112773>
43. Lautenschlaeger MP, Hasse H (2019) Transport properties of the Lennard-Jones truncated and shifted fluid from non-equilibrium molecular dynamics simulations. *Fluid Phase Equilib* 482:38–47. <https://doi.org/10.1016/j.fluid.2018.10.019>
44. Heier M, Diewald F, Horsch MT, Langenbach K, Müller R, Hasse H (2019) Molecular dynamics study of adsorption of the Lennard-Jones truncated and shifted fluid on planar walls. *J Chem Eng Data* 64(2):386–394. <https://doi.org/10.1021/acs.jced.8b00927>
45. Schmitt S, Vo T, Lautenschlaeger MP, Stephan S, Hasse H (2022) Molecular dynamics simulation study of heat transfer across solid-fluid interfaces in a simple model system. *Mol Phys* 120(10):e2057364. <https://doi.org/10.1080/00268976.2022.2057364>
46. Pharr GM, Herbert G, Gao Y (2010) The indentation size effect: a critical examination of experimental observations and mechanistic interpretations. *Annu Rev Mater Res* 40:271. <https://doi.org/10.1146/annurev-matsci-070909-104456>

47. Brodyanski A, Klein MW, Merz R, Smaga M, Beck T, Kopnarski M (2020) Microstructural changes caused by friction loading in high manganese TWIP steel and case-hardened 16MnCr5. *Mater Charact* 163:110231. <https://doi.org/10.1016/j.matchar.2020.110231>
48. Merz R, Brodyanski A, Kopnarski M (2015) On the role of oxidation in tribological contacts under environmental conditions. In: *Conference Papers in Science 2015*, p 515498. <https://doi.org/10.1155/2015/515498>
49. Huttenlochner K, Müller-Renno C, Ziegler C, Merz R, Merz B, Kopnarski M, Chodorski J, Schlegel C, Ulber R (2017) Removing biofilms from stainless steel without changing surface properties relevant for bacterial attachment. *Biointerphases* 12(2):02C404. <https://doi.org/10.1116/1.4982196>
50. Becker S, Merz R, Hasse H, Kopnarski M (2016) Solvent cleaning and wettability of technical steel and titanium surfaces. *Adsorpt Sci Technol* 34(4–5):261–274. <https://doi.org/10.1177/0263617416645110>